Arab J Sci Eng (2017) 42:2899–2914
DOI 10.1007/s13369-016-2336-7

RESEARCH ARTICLE - SYSTEMS ENGINEERING

Engine Control Design Using Compressor Guided Vanes During Autorotation Power Recovery

Fengyong Sun[1,2] · **Haibo Zhang**[1,2]

Received: 2 August 2016 / Accepted: 13 October 2016 / Published online: 31 October 2016

Abstract In order to improve the helicopter responsive ability during autorotation power recovery maneuvers, a new turbo-shaft engine control scheme is proposed in this paper. Using rotor flapping/lagging dynamics and an induced velocity model which is capable of capturing vortex ring characteristics, an integrated helicopter and engine model was developed to simulate autorotation process. By introducing a closed-loop with compressor guided vanes, a novel two-variable engine control law is devised using Linear Matrix Inequality Pole Placement method. This allows for a rapid adaptation of the helicopter to a large and fast needed torque variation required in autorotation power recovery. The transient performances and the robustness for the closed-loop helicopter-pilot system are validated for some examples appropriated to autorotation training procedure. Simulation results illustrate that, with this novel control law, the helicopter's ability to respond during autorotation is strongly enhanced when compared to traditional cases.

Keywords Helicopter · Engine · Integrated model · Autorotation · Control

List of symbols

W_f	Fuel flow rate (kg/s)
χ	Compressor guided vane angle (°)
N_g	Relative rotor speed of gas turbine (%)
N_p	Relative rotor speed of power turbine (%)
SM_c	Stall margin of compressor (%)
η_c	Efficiency of compressor (–)
V_x, V_y, V_z	Velocities along X, Y and Z axis
Ψ, Φ, Θ	Yaw, roll and pitch angle of helicopter (°)
$\theta_0, A_{1c}, B_{1s}, \theta_T$	Rotor collective, lateral cyclic pitch, longitudinal cyclic pitch (°)
p, q, r	Angular rate about X-axis, Y-axis and Z-axis with respect to b-frame (rad/s)
G	Gravity of helicopter (N)
$J_R, J_{GB}, J_{TL}, J_E, J_{acc}$	Moment of inertia of rotor, gearbox, tail rotor, engine and other accessories(kg m^2)
$\Omega_R, \Omega_E, \Omega_{GB}, \Omega_{TL}$	Main rotor speed, engine output shaft speed, Gearbox output shaft speed, tail rotor speed (rad/s)

Subscript

E	Engine
H	Helicopter
t	Total thermodynamic parameter
cor	Corrected thermodynamic parameter
ds	Design-point value

✉ Haibo Zhang
zh_zhhb@126.com

Fengyong Sun
fengyong.sun@nuaa.edu.cn

[1] Nanjing University of Aeronautics and Astronautics, Nanjing 210016, Jiangsu, People's Republic of China

[2] College of Energy and Power Engineering, Jiangsu Province Key Laboratory of Aerospace Power Systems, Nanjing, People's Republic of China

g	Earth fixed axes system
b	Airframe fixed axes system
h	Rotor hub fixed axes system

1 Introduction

Autorotation is a typical helicopter flight condition characterized by the ability of the main rotor system to sustain the rotor speed when the engines no longer transmit power to the rotor. This condition can be obtained by setting the helicopter in descent flight and extracting power from upward incoming airflow. In this way, presuming that helicopter descent rate is in a safe range necessary to initiate an autorotation procedure, a certain amount of lift can also be acquired by the spinning rotor, making the helicopter mostly a safe mean of transportation in such emergency situations. A successful autorotation ensures a safe landing; however, the complicated flow behavior around the rotor can lead to pilot difficulties in handling this maneuver. Present statistical data from AH-1, UH-2, OH-58, and OH-6 helicopters [1] show that at least one unsuccessful emergency autorotation landing happens during 10,000-h service life, this is more than 27 % of total accidents, sometimes this being accompanied by some degree of vehicle damage or personnel injury. The Federal Aviation Administration (FAA) [1] states that heavy lift rotorcrafts should be within the requirement of Category A performance during autorotation. This means that inside the flight envelope a helicopter should guarantee a continuing flight in One Engine Inoperative (OEI) or safe landing by entering autorotation in All Engines Inoperative (AEI) condition [2]. A survey made by the US Army Aviation organization [3] reveals that the pilots strongly desire to practice autorotation in flight despite the inherent safety risks. As a considerable number of accidents occurred due to engine failures (see Ref. [3]), autorotation practice is looked upon as a crucial part of the pilots training curriculum. A typical autorotation exercise mainly consists of following phases: engine failure simulation (often let engine go into idle state), autorotation entry, descent flight, steady (trimmed) autorotation and finally power recovery from the autorotation exercise, as shown in Fig. 1. In the first phase, the rotor shaft is disengaged from the free turbine output shaft via a clutch, while the engine does not really enter into malfunction but into an idle state to simulate engine failure. Next, in the autorotation's entry phase, the pilot collective pitch control is immediately lowered to delay the rotor speed decreasing and to provide enough rotor thrust to achieve a steady descent rate. Subsequently, if being successful the helicopter will enter into a steady (trimmed) autorotation phase at a certain descent rate where the rotor speed slightly changed. Finally, the recovery from the autorotation involves collective pitch flare from the pilot; therefore, the clutch is connected again when the rotor and the gear box output shaft speed remain within a small range.

For getting more feasible autorotation training control, the autorotation modeling and trajectory optimization have been tremendously studied during the past decades. And firstly, literatures about autorotation modeling are reviewed herein. Houston in Ref. [4] firstly described the coupling between the rotor speed and the longitudinal rigid body motion in autorotation. A more comprehensive rotor wake analysis described in Ref. [5] was compared to the finite-state induced velocity model. Reference [6] compared two aerodynamic models, i.e., the Pitt/Peters inflow model and a more detailed CFD model, when performing autorotation in forward flight. For simulating the vortex ring, turbulent wake and windmill brake states in autorotation, a more feasible inflow model was exploited in Ref. [7]. Similarly, a simplified ring vortex model was developed and validated for a rotor in a wide range of descent rate in Ref. [8]. Simplified vortex ring model has been successfully implemented in some helicopter models as presented in Ref. [9].

Secondly, the autorotation control after engine failure is extensively documented in the literature. Reference [10] firstly regarded the autorotation control using a two-degree-of-freedom (DOF) point-mass model of an OH-58 helicopter. Later, Aponso in Ref. [11] proposed a real-time trajectory optimization algorithm for rotorcraft autorotation training using a five-DOF rotorcraft model involving induced velocity, horizontal/vertical translations, rotor angular speed and engine power. Reference [6] demonstrated a model predictive control for autorotation based on a three DOF (descent rate, rotor speed and induced velocity) helicopter model. Reference [12] presented a four-DOF helicopter model (horizontal and vertical translations, fuselage pitch angle, and rotor angular speed) and used it to optimize helicopter trajectory during takeoff and landing after engine failure. In Ref. [13], a two-dimensional point-mass model with rotor speed and engine power dynamics model was employed with the goal to develop a control method and an algorithm for single main rotor helicopter flight after engine failure. A four-DOF helicopter model was utilized in Ref. [14] for studies of helicopter control after power failures. In Ref. [15], a four-DOF UH-60A model was employed, aiming at minimizing the size of the height–velocity diagram for safely landing without power. An eight-DOF model for the PZL Mi-2 Plus helicopter (three translations and three rotations of a rigid fuselage, main rotor speed, and engine output power) was developed to optimize autorotation profiles with different performance indices, finally comparing the results with flight test data [16]. The above-mentioned autorotation control models can be regarded as being specific for investigation of optimized profiles after engine failures; however, they are not sufficient for designing flight or engine control law during autorotation [17–21]. This motivates the need for more

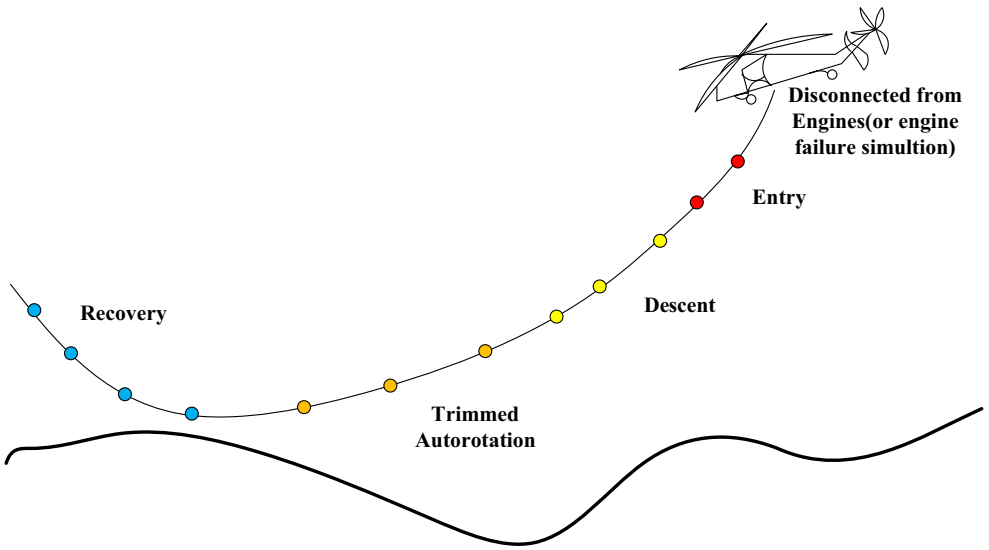

Fig. 1 Autorotation training process

specific flight dynamic models with feasibility and generality for flight controller design.

It is meaningful to emphasize the significance and necessity of autorotation power recovery simulation and control. Effective autorotation power control will guide the helicopter to a safe landing, while the engine gets into emergency state and could not restart. On the other side, excellent engine control scheme ought to consider the helicopter autorotation recovery situations. Considering the helicopter restart process is uncertain such as the flight height close to ground and the other emergency situations, engine rapid response control will contribute to the helicopter climb. Therefore, the focus of this paper is on the important control problem that the pilots will encounter different "dilemmas" during the autorotation training, especially when recovering from autorotation. When the engine goes into an idle state and cannot provide enough torque to the rotor, the significant drop of the rotor speed can result in some dangerous helicopter dynamics. Shanthakumaran et al. [22] investigated an integrated flight and engine fuel control on an Apache AH-64/T700 system and concluded that autorotation power recovery deemed the largest rotor torque variation which needed to be analyzed and controlled. Simulations showed that an unacceptable droop of the rotor speed or the free turbine speed was produced and the droop was over 5 % when the collective pitch increment rate was 29 %/s, and over 12 % when the collective pitch increment rate was 35 %/s. In Shanthakumaran's work, autorotation power recovery was simulated only related to the rotor/engine coupled system without integrating airframe dynamics. Obviously, there is a limitation to enhance the response ability of the engine with the control scheme only by fuel. Some further studies [23,24] have found that single fuel control is able to enhance the engine response ability with a look-up table adjusting by compressor guided vanes, but studies for closed-loop control by compressor guided vanes have not been implemented yet.

This paper contributes to both autorotation modeling and control by: (1) developing a detailed helicopter/engine model for accurate simulating autorotation and (2) proposing new engine control laws capable of adapting the helicopter torque to the large and fast variations characteristic during autorotation power recovery. An integrated helicopter engine model is developed in the present study for the UH-60 helicopter/T700 engine including the dynamics of the flapping angles, rotor speed, induced velocity, six DOFs of fuselage and five DOFs of engine dynamics (gas turbine rotor speed, power turbine rotor speed, total pressure of three typical volumes). This integrated model is then taken as a validation platform, being specifically improved with vortex ring induced velocity model in order to improve the accuracy of simulations in autorotation. A new engine control law is obtained by integrating compressor guided vanes closed-loop regulation with fuel flow control. The engine control law is based on Linear Matrix Inequality (LMI) pole placement method [25,26] in order to enhance the dynamic response performance during autorotation power recovery process and subsequently verified by autorotation training from an initial hovering flight.

The paper is organized as follows: The mechanism of autorotation is presented in Sect. 2. Section 3 develops an integrated helicopter and engine model to simulate autorotation and verifying the proposed control scheme. In Sect. 4, on the basis of a LMI pole placement method an engine control law using fuel flow and compressor guided vanes is proposed and implemented in autorotation. Finally, Sect. 5 conducts

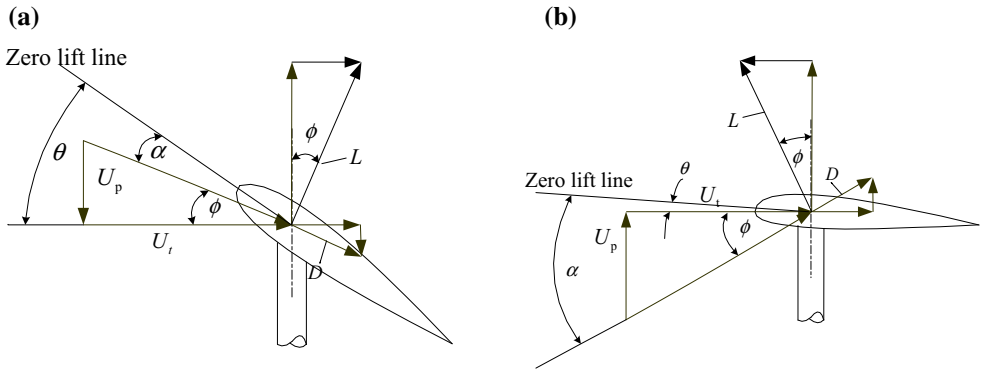

Fig. 2 Forces schematics on rotor blade element. **a** Powered flight. **b** Autorotation

different simulation cases for validating the new engine control law in autorotation training.

2 Mechanism of Autorotation

During autorotation, there is a significant difference in the aerodynamic loads of the main rotor as compared to the helicopter powered state. The mechanism of autorotation can be simply explained by forces analysis on a blade element. Figure 2a, b schematically shows the forces acting on a blade element in normal flight and autorotation, respectively. L and D represent the lift and drag force. U_p and U_t are the local air velocities in the blade segment frame which are decomposed from the coming free stream. α and θ are the angle of attack and blade pitch.

The tangential component of the velocity is $U_\mathrm{t} \approx \Omega_\mathrm{R} R_s$ (R_s is the span-wise radius of the corresponding blade element), and the perpendicular velocity is $U_\mathrm{P} \approx V_z - V_\mathrm{i}$ and $\phi = \arctan(U_\mathrm{P}/U_\mathrm{t})$. It follows that the inflow angle is negative in normal flights, and positive in autorotation. It can be seen that for a certain value of the helicopter descent rate, the component of the lift force can balance the blade profile drag force, thus allowing the rotor to achieve a steady autorotation.

3 Detailed Description of the Helicopter Model

A validated helicopter with twin engines system model depicted in [27–29] is employed for the verification and validation of the control law developed in the present study. The model is based on the Sikorsky UH-60 Black Hawk medium-lift utility helicopter developed by Sikorsky Aircraft in 1972. It features four-bladed main and tail rotors and is powered by two General Electric T700 turbo-shaft engines.

The model consists of three major parts: main rotor, airframe and engine. As shown in Fig. 3, the earth, airframe and rotor hub fixed systems are denoted as g-, b- and h-Frame, respectively.

3.1 Main Rotor Model

The main rotor of UH-60 helicopter is a single rotor type, and it is modeled based on blade element theory. The blade element relative lift and drag coefficients are provided by verified wind tunnel test data [19,20] to guarantee a considerable accuracy in the flapping dynamics equations. Moreover, the rotor moment and thrust are also numerically validated. At any azimuthal position $\psi_{\mathrm{i,i}\le N_\mathrm{b}}$, the flapping equation given in [27] is written as below:

$$\begin{aligned}\ddot{\beta}_\mathrm{i} = \frac{m_\mathrm{b}}{I_\mathrm{b}} &\left\{ \begin{array}{l} \cos\beta_\mathrm{i}\left\langle \dot{V}_z^h + \mathrm{e}\left[2\Omega_\mathrm{R}\left(p\cos\psi_\mathrm{i} - q\sin\psi_\mathrm{i}\right) + \dot{p}\sin\psi_\mathrm{i} + \dot{q}\cos\psi_\mathrm{i}\right]\right\rangle \\ \quad + \sin\beta_\mathrm{i}\left[-\dot{V}_x^h\cos\psi_\mathrm{i} + \dot{V}_y^h\sin\psi_\mathrm{i} - \mathrm{e}(r-\Omega_\mathrm{R})^2\right] \end{array} \right\} \\ &+ \cos^2\beta_\mathrm{i}\left[\dot{p}\sin\psi_\mathrm{i} + \dot{q}\cos\psi_\mathrm{i} - 2\Omega_\mathrm{R}\left(q\sin\psi_\mathrm{i} - p\cos\psi_\mathrm{i}\right)\right] \\ &- \cos\beta_\mathrm{i}\sin\beta_\mathrm{i}(r-\Omega_\mathrm{R})^2 + \frac{M_{\mathrm{flap,i}}}{I_\mathrm{b}} \end{aligned} \tag{1}$$

To simulate typical nonlinear characteristics in autorotation (such as vortex ring state), an empirical induced velocity model reported in Refs. [4,9] is used, as shown in Fig. 4. In this figure, $V_{\mathrm{i,s}}$ denotes the steady induced velocity of the rotor disc. V_z^g denotes the descent velocity. And, $V_{\mathrm{i,h}}$ denotes the baseline velocity computed from hover state actuator disc theory:

$$V_{\mathrm{i,h}} = \sqrt{\frac{G}{2\rho\pi R_m^2}} \tag{2}$$

The static induced velocity model is fitted by a 4th grade polynomial function:

$$\begin{aligned}\frac{V_{\mathrm{i,s}}}{V_{\mathrm{i,h}}} = f_\mathrm{i}\left(\frac{V_z^\mathrm{g}}{V_{\mathrm{i,h}}}\right) &= k_0 + k_1\frac{V_z^\mathrm{g}}{V_{\mathrm{i,h}}} + k_2\left(\frac{V_z^\mathrm{g}}{V_{\mathrm{i,h}}}\right)^2 \\ &\quad + k_3\left(\frac{V_z^\mathrm{g}}{V_{\mathrm{i,h}}}\right)^3 + k_4\left(\frac{V_z^\mathrm{g}}{V_{\mathrm{i,h}}}\right)^4. \end{aligned} \tag{3}$$

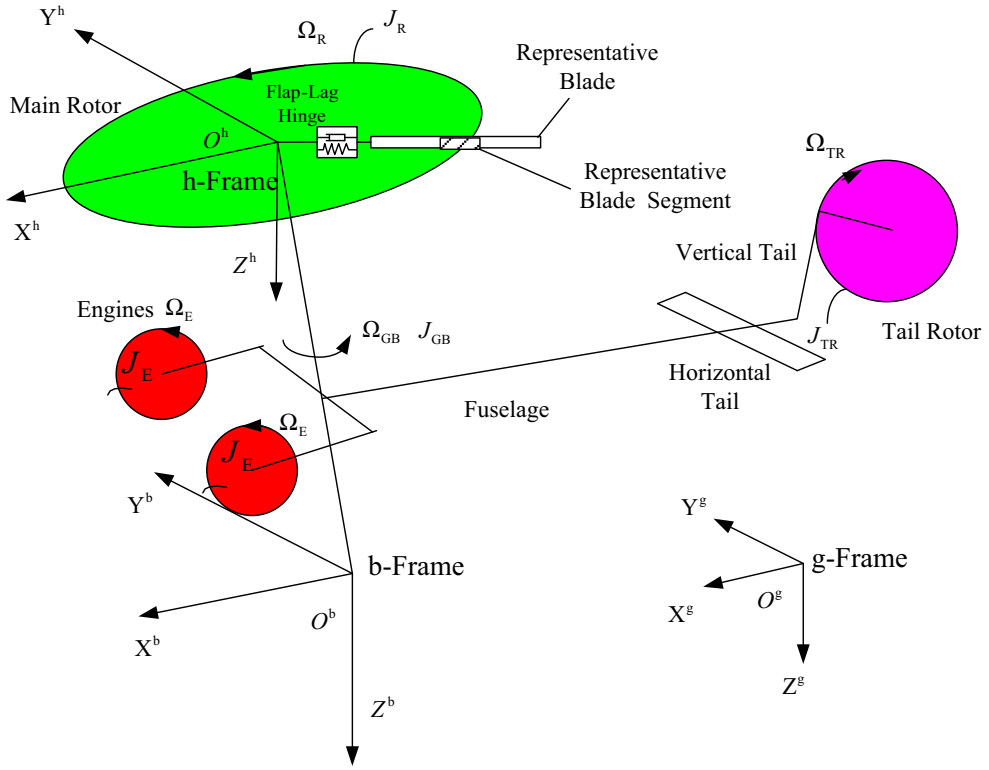

Fig. 3 Orthogonal axes system for helicopter flight dynamics

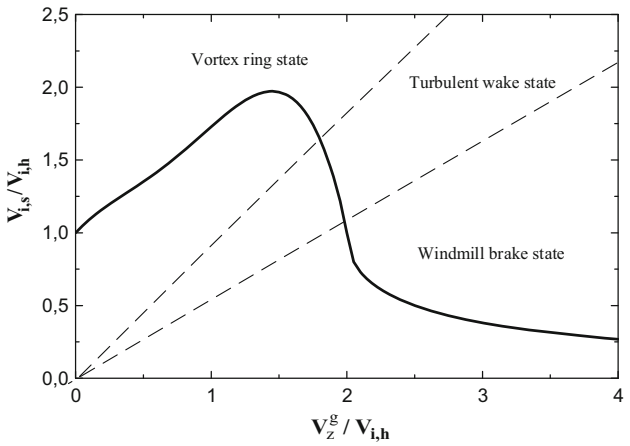

Fig. 4 Induced velocity of rotor disc as a function of descent rate

For a descent velocity smaller than the induced velocity in hover, i.e., $V_z^{\mathrm{g}} < V_{\mathrm{i,h}}$, the rotor goes into the vortex ring state. When $V_{\mathrm{i,h}} > V_z^{\mathrm{g}} > 2V_{\mathrm{i,h}}$, the rotor will be immersed into the turbulent wake state. For $V_z^{\mathrm{g}} > 2V_{\mathrm{i,h}}$ the flow field of the rotor becomes again steady and enters into autorotation state.

The following equation is used to describe the dynamics of the induced velocity:

$$\dot{V}_{\mathrm{i}} = -\frac{2.356}{R}\left(V_{\mathrm{i}}^2 - V_{\mathrm{i,s}}^2\right). \tag{4}$$

The dynamics of the rotor speed employed in this paper is adapted from Ref. [30] and is formulated as:

$$\dot{\Omega}_{\mathrm{R}} = \dot{r} + (Q_{\mathrm{E}} - Q_{\mathrm{H}})/J_{\mathrm{R}}, \tag{5}$$

where the moment of inertia of rotor $J_{\mathrm{R}} = 1.1N_{\mathrm{b}}I_{\mathrm{b}}$, and Q_{H}, Q_{E} denote the torque required by the helicopter and supplied by engine.

3.2 Airframe Model

The helicopter airframe contains several components such as fuselage, horizontal tail, vertical tail and tail rotor. The fuselage aerodynamics is modeled as a function of the body angle of attack and sideslip in the range from $-90°$ to $+90°$. The lift and the drag forces produced by the horizontal and vertical tails are computed using look-up tables with respect to fuselage angle of attack. The tail rotor model is derived from linearized Bailey theory.

Defining $\boldsymbol{x}_{\mathrm{H}} = \left(\boldsymbol{V}^{\mathrm{g}} = \begin{bmatrix} V_x^{\mathrm{g}} \\ V_y^{\mathrm{g}} \\ V_z^{\mathrm{g}} \end{bmatrix}, \boldsymbol{\omega} = \begin{bmatrix} p \\ q \\ r \end{bmatrix}, \boldsymbol{\theta} = \begin{bmatrix} \theta \\ \psi \\ \phi \end{bmatrix}\right)^{\mathrm{T}}$ and $\boldsymbol{u}_{\mathrm{H}} = (\theta_0, A_{1\mathrm{c}}, B_{1\mathrm{s}}, \theta_{\mathrm{t}})^{\mathrm{T}}$ as state and control vectors respectively, for a six-DOF rigid body the governing dynamic

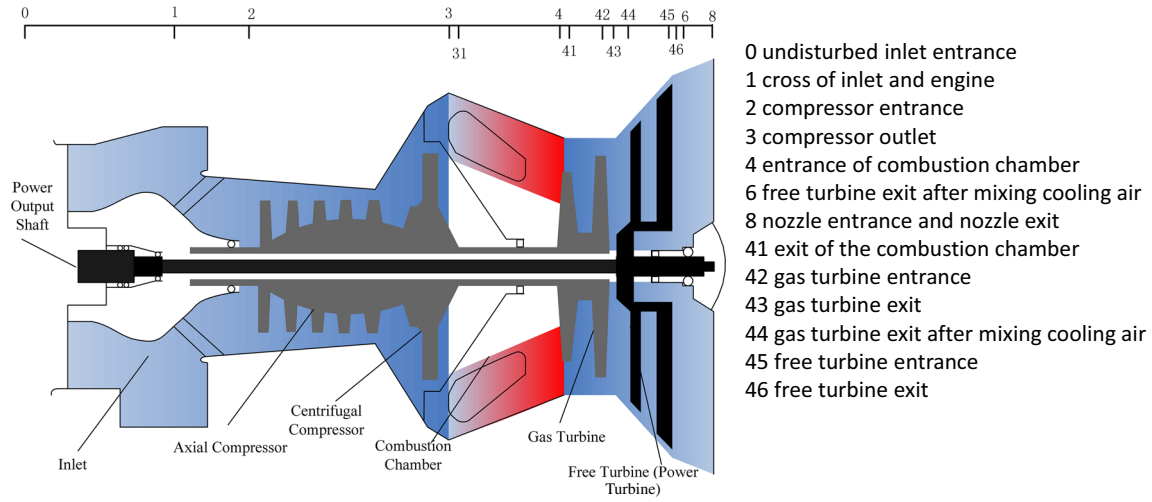

Fig. 5 T700 engine structure

equations for the airframe can be expressed as [19]:

$$\dot{\boldsymbol{x}}_{\mathrm{H}} = f_{\mathrm{H}}(\boldsymbol{x}_{\mathrm{H}}, \boldsymbol{u}_{\mathrm{H}}). \tag{6}$$

Equation (6) can be solved numerically by using a proper integration method.

3.3 Turbo-Shaft Engine Model

The T700 turbo-shaft engine contains inlet, compressor, combustion chamber, gas turbine, free turbine and nozzle as shown in Fig. 5. The compressor system consists of a five-stage axial and one-stage centrifugal compressors. This compressor system is directly linked with the gas turbine through the shaft, whereas the rotor is driven by free turbine through the power output shaft.

3.3.1 Computing of Each Component of the Engine

The engine is modeled based on component-level method introduced in Ref. [31] and using the necessary data set from Refs. [32,33]. Each engine component is sequentially modeled by virtue of its thermodynamic characteristics and coupled to rotor dynamics and working fluid flow continuity. For example, the compressor could be modeled employing a predefined performance map, which related to guided vanes could be formulated as:

$$\begin{cases} m_{\mathrm{a2cor}}, \mathrm{HPC} = f_{\mathrm{m}}\left(\pi_{\mathrm{c}}, N_{\mathrm{gcor}}, \Delta\chi\right) \\ \eta_{\mathrm{c}} = f_{\eta}\left(\pi_{\mathrm{c}}, N_{\mathrm{gcor}}, \Delta\chi\right) \end{cases} \tag{7}$$

where π_{c}, η_{c}, m_{a2cor}, N_{gcor}, χ are, respectively, the compressor pressure ratio, efficiency, corrected air flow, corrected rotor speed and guided vane angle, and HPC is power needed for compressor.

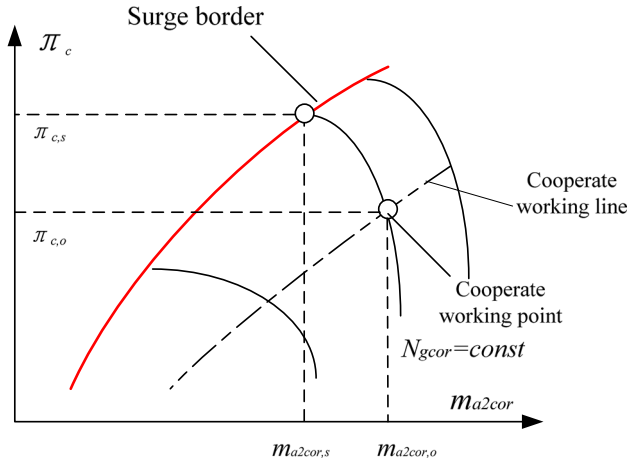

Fig. 6 Compressor performance map

Especially for a turbo-shaft engine, a surge margin concept is defined to identify the physical meaning of the relative distance existing between the cooperative working point and the surge border in the compressor performance map (see Fig. 6). This margin is used to indicate the stall margin for an engine, which is a basic control limit for acceleration. The following equation is generally used to represent the surge margin of a compressor:

$$\mathrm{SM_c} = \frac{\pi_{\mathrm{c,s}}/m_{\mathrm{a2cor,s}} - \pi_{\mathrm{c,o}}/m_{\mathrm{a2cor,o}}}{\pi_{\mathrm{c,o}}/m_{\mathrm{a2cor,o}}} = \frac{\pi_{\mathrm{c,s}}}{\pi_{\mathrm{c,o}}} \cdot \frac{m_{\mathrm{a2cor,o}}}{m_{\mathrm{a2cor,s}}} - 1$$
$$\pi_{\mathrm{c,o}} = \pi_{\mathrm{c}}, m_{\mathrm{a2cor,o}} = m_{\mathrm{a2cor}}$$

where subscripts o and s denote the relative values located in surge border and cooperating working line, respectively, along some equal N_{gcor} line. It should be observed that $\pi_{\mathrm{c,s}}$ and $m_{\mathrm{a2cor,s}}$ are also computed using Eq. (7).

3.3.2 Cooperated Working Dynamics of the Engine

Each component of the engine is cooperated through its volume main rotor dynamics. For volume dynamics, in order to describe the relationship existing between fluid flow and pressure variation, three typical volumes need to be considered as follows: (a) the combustion chamber volume-V_{Comb}, (b) the volume between the gas turbine exit and the free turn entrance-$V_{\mathrm{GTb\_PTb}}$ and (c) the nozzle volume-V_{Noz}. The volume dynamics for the engine is then expressed by the following differential equations:

$$\dot{P}_{\mathrm{t4}} = \frac{k_4 \Upsilon T_{\mathrm{t4}}}{V_{\mathrm{Comb}}}(m_{\mathrm{a3}} + W_{\mathrm{f}} - m_{\mathrm{g4}}) \tag{8}$$

$$\dot{P}_{\mathrm{t44}} = \frac{k_{44} \Upsilon T_{\mathrm{t44}}}{V_{\mathrm{GTb\_PTb}}}(m_{\mathrm{g43}} - m_{\mathrm{g44}}) \tag{9}$$

$$\dot{P}_{\mathrm{t8}} = \frac{k_8 \Upsilon T_{\mathrm{t8}}}{V_{\mathrm{Noz}}}(m_{\mathrm{g6}} - m_{\mathrm{g8}}) \tag{10}$$

where k is the gas or air adiabatic exponent at relative component section, Υ represents the gas constant and P_{t}, T_{t} denote, respectively, the total pressure and temperature at the relative component section. m_{a} is as the air mass flow at relative entrance or exit section, m_{g} is the gas mass flow at relative entrance or exit section, and W_{f} is fuel flow rate.

For the engine rotor dynamics, the following dynamic equations must be fulfilled:

$$\dot{N}_{\mathrm{g}} = \left(\frac{30}{\pi}\right)^2 \frac{(\mathrm{HPT–HPC})}{J_{\mathrm{g}} \cdot N_{\mathrm{g}}} \tag{11}$$

$$\dot{N}_{\mathrm{p}} = \left(\frac{30}{\pi}\right)^2 \frac{(\mathrm{HPA–HPP})}{J_{\mathrm{p}} \cdot N_{\mathrm{p}}} \tag{12}$$

where HPA, HPP and HPT represent power needed by helicopter, output power from power turbine, power supplied from gas turbine. Note that all parameters of HPP, HPT and HPC can be computed throughout the relative component models of the engine while HPA gotten by helicopter model.

Assuming that HPA is a disturbance imposed on the engine, the dynamics of the turbo-shaft engine can be expressed as follows:

$$\dot{\boldsymbol{x}}_{\mathrm{E}} = f_{\mathrm{E}}(\boldsymbol{x}_{\mathrm{E}}, \boldsymbol{u}_{\mathrm{E}}, \mathrm{HPA}) \tag{13}$$

where $\boldsymbol{x}_{\mathrm{E}} = [\, N_{\mathrm{g}} \;\; N_{\mathrm{p}} \;\; P_{\mathrm{t44}} \;\; P_{\mathrm{t45}} \;\; P_{\mathrm{t8}} \,]^{\mathrm{T}}$, $\boldsymbol{u}_{\mathrm{E}} = \left[\, W_{\mathrm{f}} \;\; \Delta\chi \,\right]^{\mathrm{T}}$ are defined as the state vector of engine and the control input vector, respectively.

3.4 Gear Box and Clutch Model

For simplicity, the gear box model is utilized as one order initial model reported in Ref. [22]. In fact, the clutch model used is simplified as an "on/off" logic. In practice, the clutches are connected again when the rotor speed is close enough to the gear box output shaft speed. Usually due to frictions existing in clutch, re-clutch action will have an impact on the autorotation recovery transient, but if the re-clutch logic is strictly in line with the defined profile, the influence will be little.

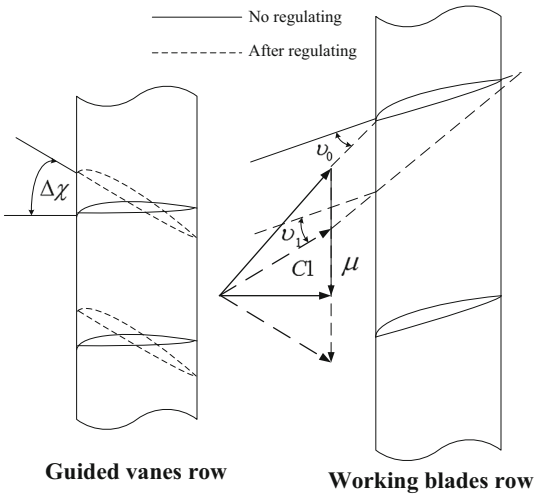

Fig. 7 Principal for compressor guided vanes regulation

4 Engine Control Law Design in Autorotation Power Recovery

4.1 Compressor Guided Vanes Control Application

The principle of compressor guided vanes regulation is presented in Fig. 7, where μ denotes the blade tip speed. The solid lines represent an off-design point for the working blades rows of the compressor guided vanes, the dotted lines show the triangle chart of the velocities in the first stage of the compressor. By adjusting the compressor guided vanes angle $\Delta\chi$, the inflow air velocity C1 of the working blades returns to working blades rotation; thus, the inflow angle υ_0 gradually decreases to υ_1 resulting in an improved compressor performance.

The compressor guided vanes angle should be therefore used as optimization parameter for improving compressor's performance in different operation modes, see Ref. [23]. Moreover, the output power can be dynamically regulated through compressor guided vanes, and the response time to load variation might be decreased with respect to the conventional single fuel flow control [23,24]. For full utilization of the two control variables containing fuel flow and compressor guided vanes of the engine control in autorotation, a robust control scheme based on pole placement in LMI regions is next developed. This guarantees that all poles of the expected closed-loop system are placed in a proper region [25,26].

This control method is capable of decreasing the conservativeness of the controller dynamic performance (this is a typical characteristic of traditional robust control), gaining better static and dynamic performance of the engine.

4.2 LMI Pole Placement Control Method

4.2.1 System Description and Transformation

Consider the following dynamic system:

$$\begin{aligned} \dot{\boldsymbol{x}} &= \boldsymbol{A}\boldsymbol{x} + \boldsymbol{B}_1\boldsymbol{w} + \boldsymbol{B}_2\boldsymbol{u} \\ \boldsymbol{y} &= \boldsymbol{C}\boldsymbol{x} + \boldsymbol{D}_{11}\boldsymbol{w} + \boldsymbol{D}_{12}\boldsymbol{u} \end{aligned} \tag{14}$$

where $\boldsymbol{x}$ denotes system state, $\boldsymbol{y}$ system output, $\boldsymbol{u}$ is the control variable, $\boldsymbol{w}$ is the system disturbance and $\boldsymbol{A}, \boldsymbol{B}_1, \boldsymbol{C}, \boldsymbol{D}_{11}, \boldsymbol{B}_2, \boldsymbol{D}_{12}$ are the corresponding matrices.

Then defining an augmented state $\bar{\boldsymbol{x}} = \left[\boldsymbol{x}^{\mathrm{T}} \ \int_0^t \boldsymbol{e}^{\mathrm{T}} d\tau\right]^{\mathrm{T}}$, the relative system is transformed to

$$\begin{aligned} \dot{\bar{\boldsymbol{x}}} &= \bar{\boldsymbol{A}}\bar{\boldsymbol{x}} + \bar{\boldsymbol{B}}_1\bar{\boldsymbol{w}} + \bar{\boldsymbol{B}}_2\bar{\boldsymbol{u}} \\ z_1 = \bar{\boldsymbol{y}} &= \bar{\boldsymbol{C}}_1\bar{\boldsymbol{x}} + \bar{\boldsymbol{D}}_{11}\bar{\boldsymbol{w}} + \bar{\boldsymbol{D}}_{12}\bar{\boldsymbol{u}} \end{aligned} \tag{15}$$

where $\bar{\boldsymbol{u}} = \boldsymbol{u}$, $\bar{\boldsymbol{w}} = \boldsymbol{w}$, $\bar{\boldsymbol{x}} = \begin{bmatrix} \dot{\boldsymbol{x}} \\ \boldsymbol{e} \end{bmatrix}$, $\bar{\boldsymbol{y}} = \boldsymbol{y}$, $\bar{\boldsymbol{A}} = \begin{bmatrix} \boldsymbol{A} & \boldsymbol{0} \\ -\boldsymbol{C} & \boldsymbol{0} \end{bmatrix}$, $\bar{\boldsymbol{B}}_1 = \begin{bmatrix} \boldsymbol{B}_1 \\ -\boldsymbol{D}_{11} \end{bmatrix}$, $\bar{\boldsymbol{B}}_2 = \begin{bmatrix} \boldsymbol{B}_2 \\ -\boldsymbol{D}_{12} \end{bmatrix}$, $\bar{\boldsymbol{C}}_1 = \begin{bmatrix} \boldsymbol{C} & \boldsymbol{0} \end{bmatrix}$, $\bar{\boldsymbol{D}}_{11} = \boldsymbol{D}_{11}$, and $\bar{\boldsymbol{D}}_{12} = \boldsymbol{D}_{12}$.

Defining $z_2 = \bar{\boldsymbol{C}}_2\bar{\boldsymbol{x}} + \bar{\boldsymbol{D}}_{22}\bar{\boldsymbol{u}}$, Eq. (15) can be rewritten as:

$$\begin{aligned} \dot{\bar{\boldsymbol{x}}} &= \bar{\boldsymbol{A}}\bar{\boldsymbol{x}} + \bar{\boldsymbol{B}}_1\bar{\boldsymbol{w}} + \bar{\boldsymbol{B}}_2\bar{\boldsymbol{u}} \\ z_1 &= \bar{\boldsymbol{C}}_1\bar{\boldsymbol{x}} + \bar{\boldsymbol{D}}_{11}\bar{\boldsymbol{w}} + \bar{\boldsymbol{D}}_{12}\bar{\boldsymbol{u}} \\ z_2 &= \bar{\boldsymbol{C}}_2\bar{\boldsymbol{x}} + \bar{\boldsymbol{D}}_{22}\bar{\boldsymbol{u}} \end{aligned} \tag{16}$$

where $\bar{\boldsymbol{C}}_2 = \begin{bmatrix} \boldsymbol{Q}^{1/2} \\ \boldsymbol{0} \end{bmatrix}$, $\bar{\boldsymbol{D}}_{22} = \begin{bmatrix} \boldsymbol{0} \\ \boldsymbol{R}^{1/2} \end{bmatrix}$, $\boldsymbol{Q} = \boldsymbol{Q}^{\mathrm{T}} \geq \boldsymbol{0}$, $\boldsymbol{R} = \boldsymbol{R}^{\mathrm{T}} > \boldsymbol{0}$ are adjustable weighted matrices.

4.2.2 Controller Design Using LMI Pole Placement Method

This method is used to design a controller with the following conditions:

Besides the $w \to z_1$ transfer function matrix H_∞ index of $\left\|T_{wz_1}(s)\right\|_\infty \leq \gamma$ and the $w \to z_2$ transfer function matrix H_2index of $\left\|T_{wz_2}(s)\right\|_2 \leq \eta$ where η, γ, are some specific positive scalar, respectively, the poles of the designed closed-loop system must be placed in the shaded cone region in Fig. 8, guaranteeing that the system has the minimal attenuation degree τ, the minimal damping ratio $\zeta = \cos\delta$ and the maximal natural angular frequency $w_{\mathrm{n}} = \varepsilon \sin\delta$. All these indexes make the overshoot, decay time and the stable time of the designed system to be confined in an expected scope.

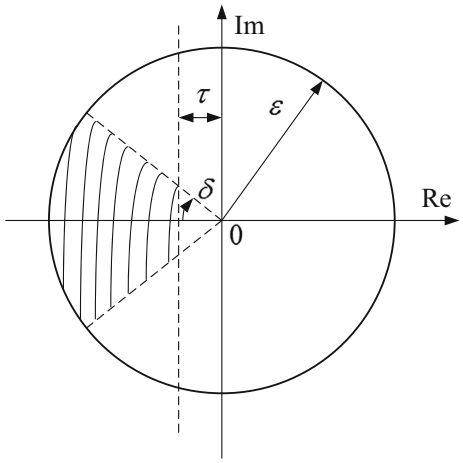

Fig. 8 The aimed cone region in LMI pole placement

Next, providing a H_2/H_∞ state feedback control law can be expressed as:

$$\bar{\boldsymbol{u}} = \bar{\boldsymbol{K}}\bar{\boldsymbol{x}} = [\boldsymbol{K}_x \ \boldsymbol{K}_e] \begin{bmatrix} \boldsymbol{x} \\ \int_0^t \boldsymbol{e}\mathrm{d}\tau \end{bmatrix} = [\boldsymbol{K}_x \ \boldsymbol{K}_e] \begin{bmatrix} \boldsymbol{x} \\ \int_0^t (\boldsymbol{r} - \boldsymbol{y})\mathrm{d}\tau \end{bmatrix}$$

where $\boldsymbol{r}$ is reference signal, and $\boldsymbol{e}$ is deviation vector between $\boldsymbol{r}$ and $\boldsymbol{y}$.

For a system as described in Eq. (16) and its state feedback control, the system matrix of the designed loop system would be $\boldsymbol{A}_c = \bar{\boldsymbol{A}} + \bar{\boldsymbol{B}}_2\bar{\boldsymbol{K}}$.

First, for corresponding to the H_∞ index needed above that $\left\|T_{wz_1}(s)\right\|_\infty \leq \gamma$, the necessary LMIs must be held as:

$$\begin{aligned} &\begin{bmatrix} \bar{\boldsymbol{A}}\bar{\boldsymbol{X}} + \bar{\boldsymbol{B}}_2\bar{\boldsymbol{Y}} + (\bar{\boldsymbol{A}}\bar{\boldsymbol{X}} + \bar{\boldsymbol{B}}_2\bar{\boldsymbol{Y}})^{\mathrm{T}} & \bar{\boldsymbol{B}}_1 & (\bar{\boldsymbol{C}}_1\bar{\boldsymbol{X}} + \bar{\boldsymbol{D}}_{12}\bar{\boldsymbol{Y}})^{\mathrm{T}} \\ \bar{\boldsymbol{B}}_1^{\mathrm{T}} & -\gamma\boldsymbol{I} & \bar{\boldsymbol{D}}_{11}^{\mathrm{T}} \\ \bar{\boldsymbol{C}}_1\bar{\boldsymbol{X}} + \bar{\boldsymbol{D}}_{12}\bar{\boldsymbol{Y}} & \bar{\boldsymbol{D}}_{11} & -\gamma\boldsymbol{I} \end{bmatrix} < 0 \\ &\begin{bmatrix} \boldsymbol{M} & \bar{\boldsymbol{C}}_2\bar{\boldsymbol{X}} + \bar{\boldsymbol{D}}_{22}\bar{\boldsymbol{Y}} \\ (\bar{\boldsymbol{C}}_2\bar{\boldsymbol{X}} + \bar{\boldsymbol{D}}_{22}\bar{\boldsymbol{Y}})^{\mathrm{T}} & \bar{\boldsymbol{X}} \end{bmatrix} > 0 \\ &\begin{bmatrix} -\varepsilon\bar{\boldsymbol{X}} & \bar{\boldsymbol{A}}\bar{\boldsymbol{X}} + \bar{\boldsymbol{B}}_2\bar{\boldsymbol{Y}} \\ (\bar{\boldsymbol{A}}\bar{\boldsymbol{X}} + \bar{\boldsymbol{B}}_2\bar{\boldsymbol{Y}})^{\mathrm{T}} & -\varepsilon\bar{\boldsymbol{X}} \end{bmatrix} < 0 \\ &\gamma < \gamma_0 \end{aligned} \tag{17}$$

where $\bar{\boldsymbol{X}}$, $\bar{\boldsymbol{Y}}$ and $\boldsymbol{M}$ are proper dimensions matrices and γ is a positive scalar.

Second, for $\left\|T_{wz_2}(s)\right\|_2 \leq \eta$ another LMI must be satisfied as:

$$\min_{\gamma, \bar{\boldsymbol{X}}, \boldsymbol{Y}, \boldsymbol{M}} \quad \alpha\gamma + \beta\mathrm{Trace}(\boldsymbol{M}) \tag{18}$$

Finally, the following LMIs give a sufficient and necessary condition for all the poles of $\boldsymbol{A}_c$ to be placed within the sector region plotted in Fig. 8.

$$\bar{A}\bar{X} + \bar{B}_2\bar{Y} + \left(\bar{A}\bar{X} + \bar{B}_2\bar{Y}\right)^{\mathrm{T}} + 2\tau\bar{X} < 0$$
$$\begin{bmatrix} -\varepsilon\bar{X} & \bar{A}\bar{X} + \bar{B}_2\bar{Y} \\ (\bar{A}\bar{X} + \bar{B}_2\bar{Y})^{\mathrm{T}} & -\varepsilon\bar{X} \end{bmatrix} < 0$$
$$\begin{bmatrix} \Lambda_1 & \Lambda_2 \end{bmatrix} < 0 \tag{19}$$

where $Y = \bar{K}\bar{X}$, $\Lambda_1 = \begin{bmatrix} \sin\delta\left[\bar{A}\bar{X}+\bar{B}_2\bar{Y}+(\bar{A}\bar{X}+\bar{B}_2\bar{Y})^{\mathrm{T}}\right] \\ \cos\delta\left[(\bar{A}\bar{X}+\bar{B}_2\bar{Y})^{\mathrm{T}}-\bar{A}\bar{X}+\bar{B}_2\bar{Y}\right] \end{bmatrix}$,
$\Lambda_2 = \begin{bmatrix} \cos\delta\left[\bar{A}\bar{X} + \bar{B}_2\bar{Y} - (\bar{A}\bar{X} + \bar{B}_2\bar{Y})^{\mathrm{T}}\right] \\ \sin\delta\left[\bar{A}\bar{X} + \bar{B}_2\bar{Y} + (\bar{A}\bar{X} + \bar{B}_2\bar{Y})^{\mathrm{T}}\right] \end{bmatrix}$.

Thus, by designating the parameters $\gamma_0, \eta_0, \alpha, \beta, \alpha_2, r$ and θ, if there exists a group of optimum solution ($\gamma^*, \bar{X}^*, \bar{Y}^*, M^*$) for the above LMIs, the state feedback control law can be derived as:

$$\bar{u} = Y^*\left(\bar{X}^*\right)^{-1} = \bar{K}\bar{x} = \begin{bmatrix} K_x & K_e \end{bmatrix}\begin{bmatrix} x \\ \int_0^t e\,\mathrm{d}\tau \end{bmatrix} \tag{20}$$

Necessity and sufficient proofs for Eqs. (17–19) can be found in Ref. [23], so they are omitted here.

However, one focuses on the asymptotic performance for tracking reference signal. For a real plant, nonlinear difference should be considered, so the following equation could be obtained from Eq. (14):

$$\dot{x} = Ax + \Delta_1(x,u) + B_1 w + B_2 u$$
$$y = Cx + \Delta_2(\mathrm{x}, u) + D_{11}w + D_{12}u \tag{21}$$

Supposing an augmented state $\bar{x} = \begin{bmatrix} x^{\mathrm{T}} & \int_0^t e^{\mathrm{T}}\mathrm{d}\tau \end{bmatrix}^{\mathrm{T}}$, the relative system (21) is transformed to:

$$\dot{\bar{x}} = \bar{A}\bar{x} + \bar{\Delta}_1(\bar{x}, \bar{u}) + \bar{B}_1\bar{w} + \bar{B}_2\bar{u}$$
$$z_1 = \bar{y} = \bar{C}_1\bar{x} + \bar{\Delta}_2(\bar{x}, \bar{u}) + \bar{D}_{11}\bar{w} + \bar{D}_{12}\bar{u} \tag{22}$$

where $\bar{\Delta}_1(\bar{x}, \bar{u}) = \begin{bmatrix} \Delta_1(x,u) \\ -\Delta_2(x,u) \end{bmatrix}$, $\bar{\Delta}_2(\bar{x}, \bar{u}) = \Delta_2(x,u)$.

Generally for helicopter aero engines, a bounded condition is guaranteed in a specific flight envelope around the trimmed state [34]:

$$\left\| \begin{bmatrix} \Delta_1(x,u) \\ \Delta_2(x,u) \end{bmatrix} \right\|_\infty < +\infty$$

Based on the lemma proposed in Ref. [35], for Eq. (21) a relative regulator derived using Eq. (20) can guarantee that all states converge to a bounded area, that is:

$$\|\bar{x}\|_\infty = \left\| \begin{bmatrix} x^{\mathrm{T}} & \int_0^t e^{\mathrm{T}}\mathrm{d}\tau \end{bmatrix}^{\mathrm{T}} \right\|_\infty < +\infty.$$

This means that $e \in L_\infty$. Furthermore, $e \in L_2$ and $e \in C^1$ could be also guaranteed in the cases of helicopters and engines. Therefore, based on *Babalat* lemma [36], the output can track the input command with the following limit conditions:

$$\lim_{t\to\infty} e = \lim_{t\to\infty}(r - y) = 0.$$

4.3 Design for Turbo-Shaft Engine Controller in Autorotation

Regarding the integrated helicopter–engine model as the controlled plant, the engine control scheme is depicted in Fig. 9, where N_{pr} denotes free turbine speed reference, N_{gr} represents gas turbine reference signal.

During the autorotation power recovery, the helicopter torque load undergoes the most violent changes, with highest amplitude peaks. Therefore, a two-variable control law containing fuel flow and compressor guided vanes is employed in describing the autorotation power recovery, which is in order to enhance the disturbance sensitivity of the closed-loop system (traditional signal loop fuel flow control law is still used in all other stages of the autorotation). During the autorotation power recovery, once the rotor speed and free turbine speed are closed enough in value, the clutch will engage again. At this time, engine should quickly supply power so as to keep the helicopter in steady state, otherwise an unacceptable rotor speed droop will develop and lead to an unsafe autorotation. Thus, as discussed above, with the help of guided vanes, the above-given two-variable control law may improve the helicopter response during autorotation.

On the basis of LMI pole placement method, the engine control can be realized, whether it is a double or a single variable control law. The definitions of the control law are denoted in Table 1.

First, a linear time invariant model (LTI) at a baseline operation point ($H = 0$ m, $V_x = 0$ m/s) is obtained using system identification methods reported in Ref. [31]. The LTI model for T700 engine is described as:

$$A_{\mathrm{E}} = \begin{bmatrix} -0.2222 & 1.4943 \\ 0.1686 & -4.1027 \end{bmatrix}, B_{\mathrm{E1}} = \begin{bmatrix} -0.1939 \\ 0.1224 \end{bmatrix},$$
$$B_{\mathrm{E2}} = \begin{bmatrix} 0.0123 & -0.2332 \\ 0.6116 & 0.8281 \end{bmatrix}$$
$$C_{\mathrm{E}} = \begin{bmatrix} 1 & 0 \\ 0 & 1 \end{bmatrix}, D_{\mathrm{E11}} = \begin{bmatrix} 0 \\ 0 \end{bmatrix}, D_{\mathrm{E12}} = \begin{bmatrix} 0 & 0 \\ 0 & 0 \end{bmatrix}.$$

After choosing appropriate design parameters, the controller gains can be derived as:

$$K_{\dot{x}} = \begin{bmatrix} 16.4826 & 4.1696 \\ -8.2031 & 4.0833 \end{bmatrix}, K_e = \begin{bmatrix} -16.2114 & -2.9005 \\ 7.0866 & -12.0657 \end{bmatrix}$$

Consequently, while considering some real constrains like surge margin, the engine control law could be formulated as:

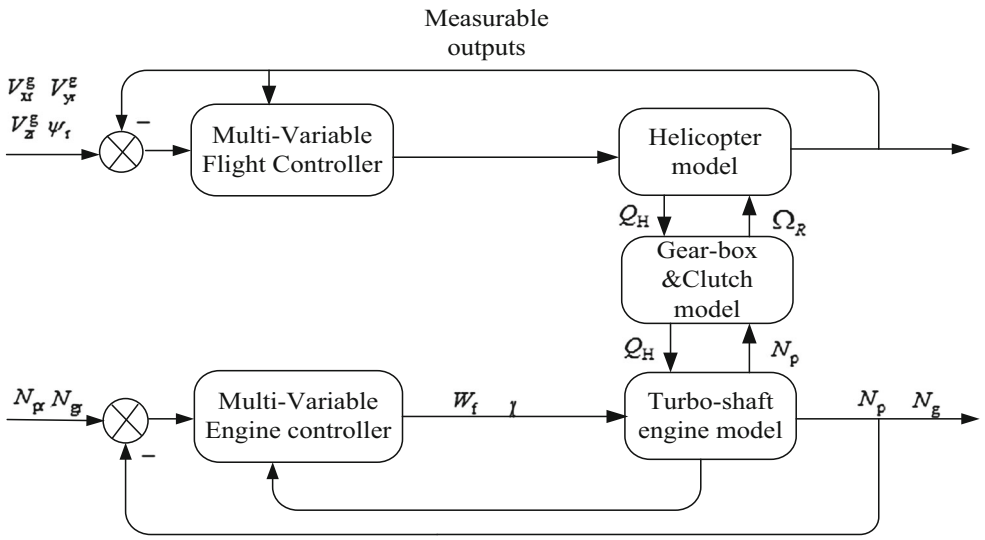

Fig. 9 A sketch for the new engine control law

Table 1 Definitions for engine control system in autorotation

System parameter definition	Expressions
State vector	$\boldsymbol{x}_{\mathrm{E}} = \left[\, N_{\mathrm{p}} \;\; N_{\mathrm{g}} \,\right]^{\mathrm{T}}$
Control vector	$\boldsymbol{u}_{\mathrm{E}} = \left[\, W_{\mathrm{f}} \;\; \Delta\chi \,\right]^{\mathrm{T}}$ or $\boldsymbol{u}_{\mathrm{E}} = W_{\mathrm{f}}$ for single fuel control
Output vector	$\boldsymbol{y}_{\mathrm{E}} = \left[\, N_{\mathrm{p}} \;\; N_{\mathrm{g}} \,\right]^{\mathrm{T}}$
Reference signal	$\boldsymbol{r}_{\mathrm{E}} = \left[\, N_{\mathrm{pr}} \;\; N_{\mathrm{gr}} \,\right]^{\mathrm{T}}$ or $\boldsymbol{r}_{\mathrm{E}} = N_{\mathrm{pr}}$ for single fuel control
Output error vector	$\boldsymbol{e}_{\mathrm{E}} = \boldsymbol{r}_{\mathrm{E}} - \boldsymbol{y}_{\mathrm{E}}$
Disturbance	$\boldsymbol{w}_{\mathrm{E}} = Q_{\mathrm{H}}$

$$\begin{cases} \boldsymbol{u}_{\mathrm{E}} = \boldsymbol{K}_{\mathrm{e}} \int_o^t \boldsymbol{e}_{\mathrm{E}} \mathrm{d}\tau + \boldsymbol{K}_{\dot{x}} \boldsymbol{x}_{\mathrm{E}}, \boldsymbol{u}_{\mathrm{E}} \le \boldsymbol{u}_{\mathrm{Elimt}} \\ \mathrm{SM_c} \ge \mathrm{SM_{c_{limit}}} \\ T_4 \le T_{4\mathrm{limit}} \\ P_3 \le P_{3\mathrm{limit}} \end{cases} \tag{23}$$

where the subscript "limit" means a limit for each parameter, $\mathrm{SM_c} \ge \mathrm{SM_{c_{limit}}}$ is related to the acceleration limit, and $T_4 \le T_{4\mathrm{limit}}$ and $P_3 \le P_{3\mathrm{limit}}$ are the limitation control limits for engine life time. Due to the latter two limits activated normally in engine maximum power state as $N_{\mathrm{g}} \approx 100\,\%$, this paper concentrates on how to improve the fast response potential of the engine, so only $\mathrm{SM_c} \ge \mathrm{SM_{c_{limit}}}$ and $\boldsymbol{u}_{\mathrm{E}} \le \boldsymbol{u}_{\mathrm{Elimt}}$ would be checked in the following validation cases.

Finally, in order to overcome the difficulties of wind up of the guided vanes' control signals, an anti-windup control law is also derived and integrated with the above two-variable engine control law.

Table 2 Definitions for flight control system in autorotation

System parameter definition	Expressions
State vector	$\boldsymbol{x}_{\mathrm{H}} = [\, V_x^{\mathrm{g}} \;\; V_y^{\mathrm{g}} \;\; V_z^{\mathrm{g}} \;\; p \;\; q \;\; r \;\; \phi \;\; \psi \;\; \theta \,]^{T}$
Control vector	$\boldsymbol{u}_{\mathrm{H}} = [\, \theta_0 \;\; A_{1c} \;\; B_{1s} \;\; \theta_t \,]^{\mathrm{T}}$
Output vector	$\boldsymbol{y}_{\mathrm{H}} = [\, V_x^{\mathrm{g}} \;\; V_y^{\mathrm{g}} \;\; V_z^{\mathrm{g}} \;\; \psi \,]^{\mathrm{T}}$
Reference signal	$\boldsymbol{r}_{\mathrm{H}} = [\, V_{x\mathrm{r}}^{\mathrm{g}} \;\; V_{x\mathrm{r}}^{\mathrm{g}} \;\; V_{x\mathrm{r}}^{\mathrm{g}} \;\; \psi_{\mathrm{r}} \,]^{\mathrm{T}}$
Output error vector	$\boldsymbol{e}_{\mathrm{H}} = \boldsymbol{r}_{\mathrm{H}} - \boldsymbol{y}_{\mathrm{H}}$
Disturbance	$\boldsymbol{w}_{\mathrm{H}} = \Omega_{\mathrm{R}}$

4.4 Design of a Helicopter Flight Controller in Autorotation

Although there is no power in autorotation, the flight control law for the UH-60 helicopter or an auto-pilot control law can also be derived based on the LMI pole placement control method. The system's states, control inputs, system outputs, etc. are given in Table 2.

In the trimmed autorotation at $H = 650\,\mathrm{m}$ and $V_z^{\mathrm{g}} = -10\,\mathrm{m/s}$, the helicopter system's matrices can be identified using perturbation method [37]. Thus, the control law for the integrated helicopter–engine system can be expressed as:

$$\boldsymbol{u}_{\mathrm{H}} = \mathbf{K}_{\mathrm{x}} \boldsymbol{x}_{\mathrm{H}} + \mathbf{K}_{\mathrm{e}} \int_{\mathbf{0}}^{\mathbf{t}} \boldsymbol{e}_{\mathrm{H}} \mathbf{d}\boldsymbol{\tau}.$$

5 Validations and Discussion

In this section, the feasibility and robustness of the two-variable control law including fuel flow and compressor guided vane angle are exemplified (in the figures, notation

Table 3 Control limits for helicopter and engine

System	System	Limits	
		Up	Low
Engine	W_f	0.08	0
	$\Delta\chi$	+6	−6
Helicopter	θ_0	18.3	0
	θ_T	36.5	4.5
	A_{1c}	8.0	−8.0
	B_{1s}	8.0	−8.0

"−D" represents the two-variable control and "−S" the single fuel flow control). The control limits imposed on the variables used in the analyzed simulation cases are listed in Table 3.

5.1 A Simulation Case for Autorotation Training

The autorotation is initialized from a hover state where $H = 650\,\text{m}$, $V_x^g = V_y^g = V_z^g = 0$ and the power recovery height is $H = 0\,\text{m}$ (Fig. 10a). At time $t = 0\,\text{s}$, the helicopter is disconnected from the engines by the clutches. As a result, the engines run quickly into the idle state in which the core compressor speed N_g is about 75 % to its design value, whereas the free turbine speed N_p has to be always kept constant via an engine controller (see Fig. 10b). For preventing the main rotor speed N_R from the severe deceleration (see Fig. 10b), and for implementation of a successful autorotation, all four control inputs of the helicopter should be adjusted appropriately by the auto-pilot control law. Using this auto-pilot control, the main rotor collective pitch θ_0 is decreased (Fig. 10c), subsequently at around $t = 6\,\text{s}$ an acceleration for the main rotor speed is realized as depicted in Fig. 10b. Meanwhile, see Fig. 10d, the helicopter torque Q_H tends to approach zero value at the beginning of the autorotation, resulting in a similar tendency for the tail rotor collective pitch, see Fig. 10c. Moreover, a negative value for Q_H as seen in Fig. 10d is an explanation for the accelerating tendency of the main rotor. This is also true when Q_H is again near zero at about $t = 20\,\text{s}$ in steady autorotation, where N_R no longer varies or changes very slowly (in this case, around 117 % nominal rpm). Obviously, the steady autorotation is acquired through a large descent velocity V_z^g as much as -18m/s, while the pilot is keeping other flight controlled variables (V_x^g, V_y^g, ψ in Fig. 10f) constant by slightly adjustments in the longitudinal cyclic A_{1c} and lateral cyclic B_{1s} as indicated in Fig. 10e.

When $t = 38\,\text{s}$, the recovery from autorotation is initiated via a fast increase of the main rotor collective pitch, the clutch is engaged again when the rotor speed is very close to the free turbine speed. Then, a large torque load from helicopter is simultaneously needed to recover to the normal flight state. Therefore, the engine, starting up from its idle state once more, is forced to output power (depicted in Fig. 10d) to the helicopter by the fuel flow W_f as shown in Fig. 10g. For obtaining a smooth fuel flow control, the compressor guided vane $\Delta\chi$ represented in Fig. 10h needs also to be adjusted to get proper air flow and compressor efficiency. Figure 10i demonstrates a validation of the explanation in Fig. 2, in which the U_p is always positive from the moment of 6 s until the full recovery, indicating that the lift along the rotor circumferential direction is able to exceed the drag force and thus accelerate the blade, ultimately reaching a balance due to aerodynamic damping. In order to validate the induced velocity model which was extended to include typical vortex ring state, Fig. 10j gives the changes in the induced velocity V_i. The obvious vortex ring behavior can be seen when entering into or recovering from the autorotation.

5.2 Validation for New Engine Control in Autorotation Power Recovery

The two-variable engine control law proposed in this paper is compared to the traditional single fuel flow control. As initial condition, the ($H = 700\,\text{m}$, $V_x^g = 10\,\text{m/s}$) point is used for autorotation training process. The single fuel flow control law is derived using the following robust control method:

$$\boldsymbol{W}_f = \boldsymbol{K}_e \int_o^t \boldsymbol{e}_E \mathrm{d}\tau + \boldsymbol{K}_x \boldsymbol{x}_E$$

where $\boldsymbol{e}_E$ and $\boldsymbol{x}_E$ are, respectively, the state vector of engine and control input vector. The relative controller gains are modulated as:

$$\boldsymbol{K}_x = \begin{bmatrix} 3.2972 & 0.8339 \end{bmatrix}, \quad \boldsymbol{K}_e = -3.2422.$$

when entering into steady-state autorotation, the engine control scheme is switched to the two-variable control law. At $t = 37\,\text{s}$, a sudden increment in pilot collective pitch input is initiated in order to achieve autorotation power recovery (Fig. 11a). This is accompanied by a reduction of rotor speed (see Fig. 11b). Similar to the above-given example, when the rotor speed approaches the value of the free turbine speed, the clutch is geared. Meanwhile, the compressor rotor speed increases rapidly for meeting the torque needed by the helicopter. Note that if the output torque cannot fulfill the helicopter rotor demand in time, a large droop in rotor speed or free turbine speed is reached. Specifically, the slower the engine supplies output torque, the larger the droop rotor speed or free turbine becomes. This can be explained also from Eq. (5). One can clearly see in Fig. 11c that the relative speed droop is less than 3 % when using compressor guide vanes regulation, and this is far more reduced than that under

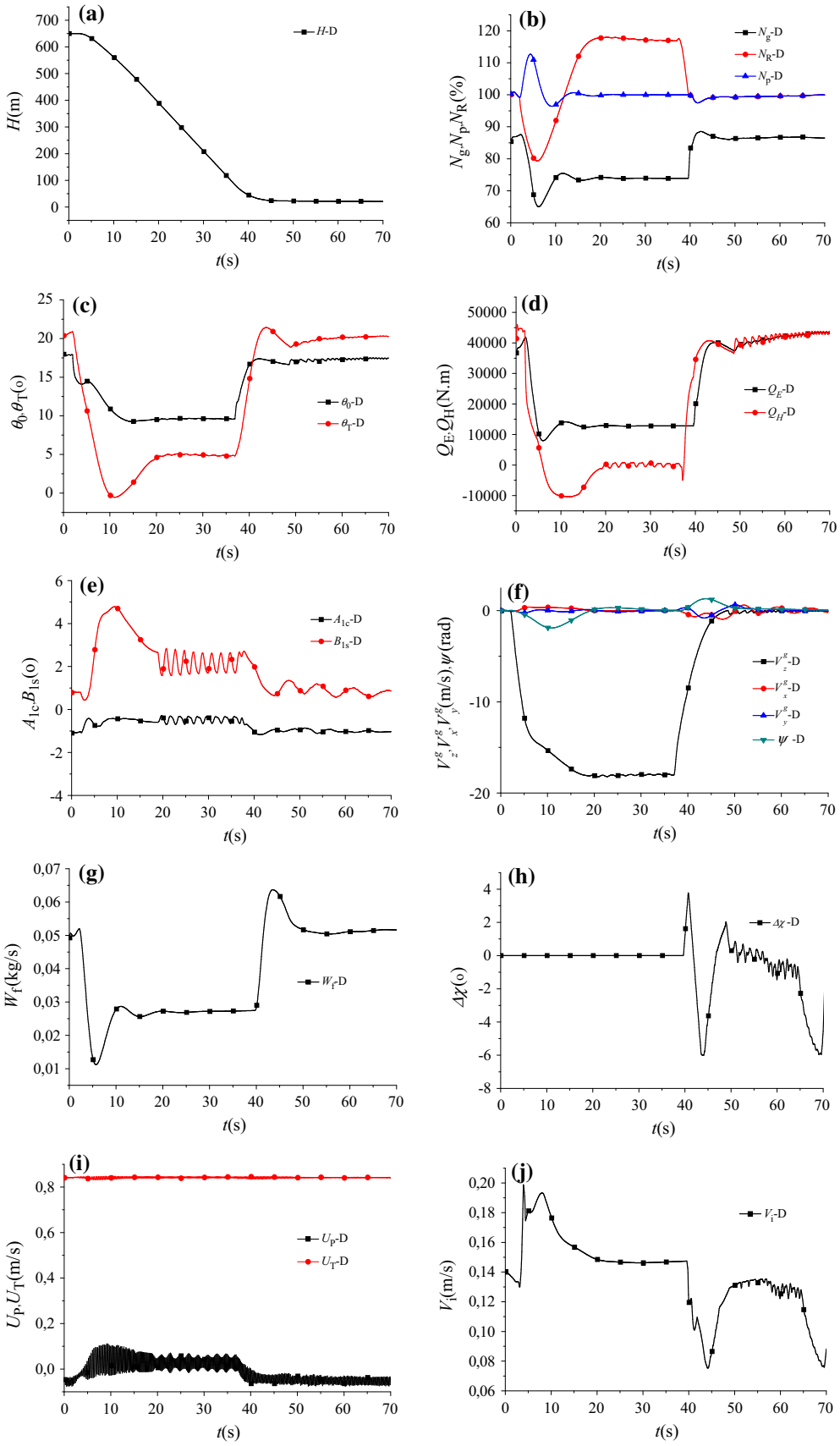

Fig. 10 An autorotation training process

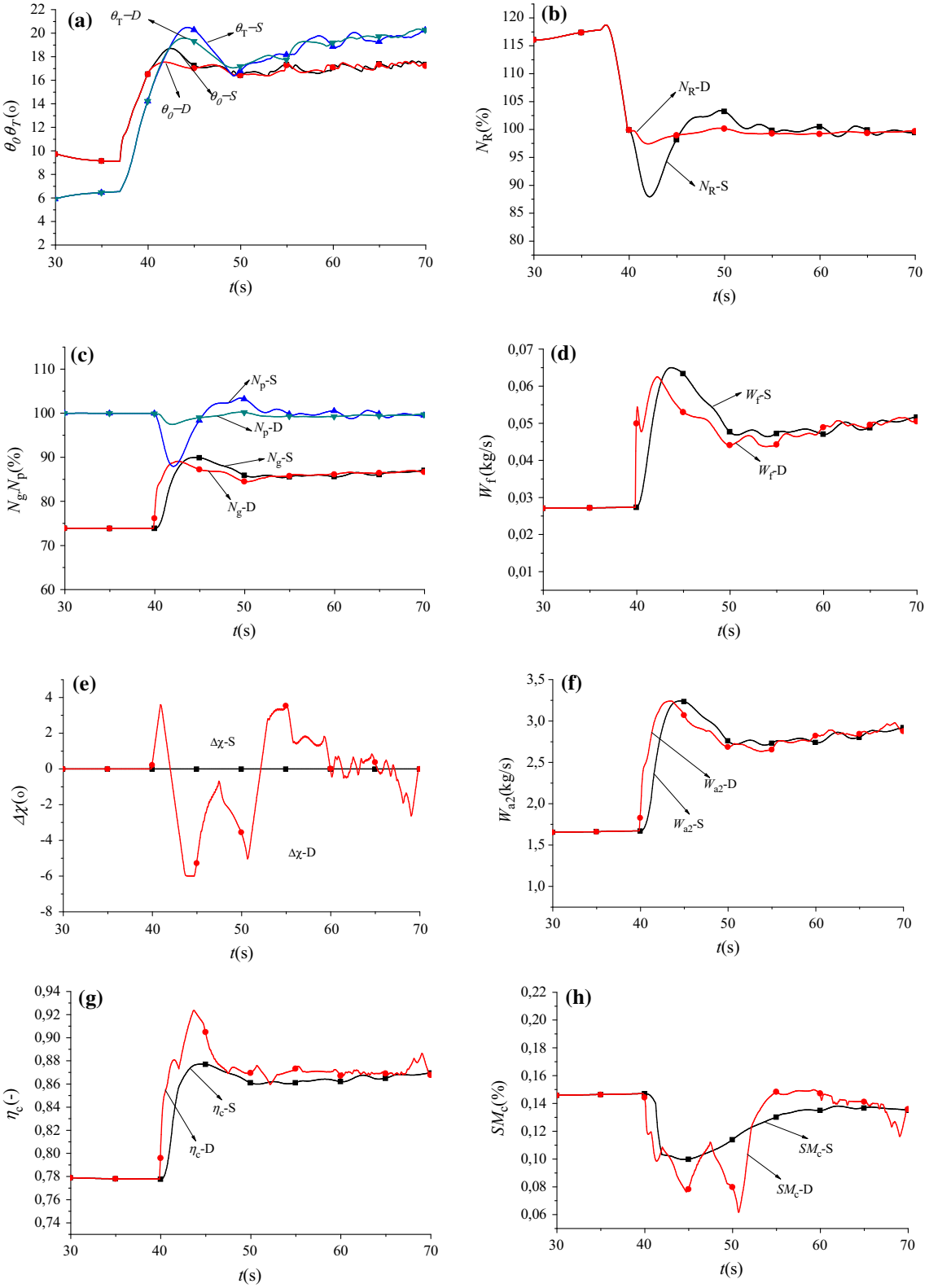

Fig. 11 Comparisons between double variable control and single fuel control

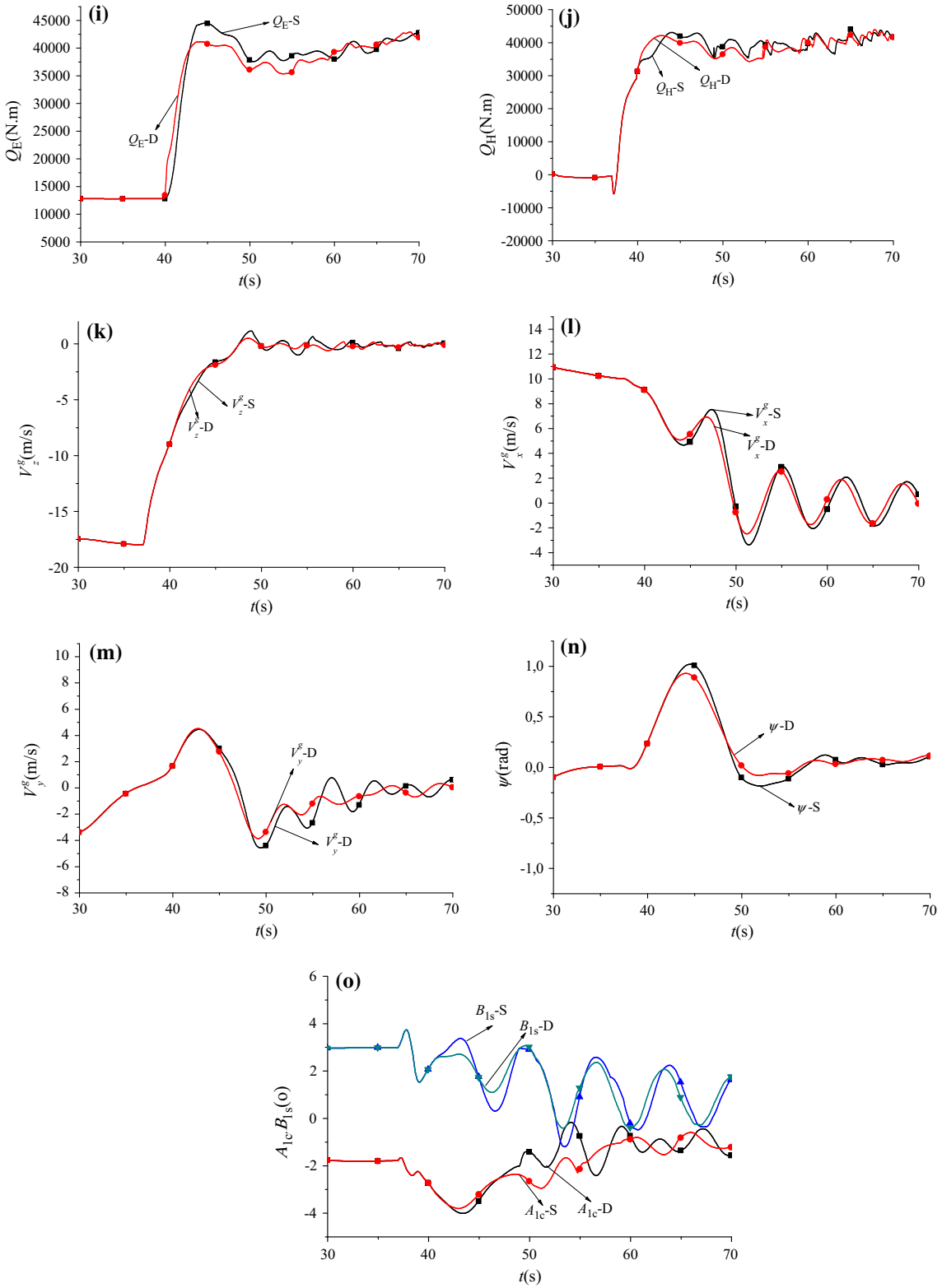

Fig. 11 continued

single fuel control. Although the amplitude of the fuel flow is smaller using the "−D" control scheme (Fig. 11d), the regulation of the compressor guided vanes as plotted in Fig. 11e shows the beneficial changes in the air flow and the compressor efficiency (Fig. 11g, h). Specifically, the regulation of the compressor guided vanes ensures a higher sensitivity to load torque from helicopter. Furthermore, the torque output from engine and compressor rotor speed explain this clear (see Fig. 11i, c); thus, this is more adaptable to the torque needed from the helicopter (see Fig. 11j). In the transient process of the compressor guided vanes regulation, a small increment of $\Delta\chi$ can be seen in the first few seconds $t = 40$ to 42 s. And, it is necessary to adapt the increasing need for the rotor speed, which is followed by a rapid decease of $\Delta\chi$ at $t = 42$ s to arrive at a more efficient compressor state after that in Fig. 11e). To eliminate the deviation of the compressor speed from the reference to the real value, a steady adaptation process is initiated after that. It is noted that compressor regulation also brings a small negative influence on the compressor stall margin as depicted in Fig. 11h, and nevertheless, the reduction is within a safety region as referred to Fig. 6, where one can see that efficiency is often higher near the surge border than that beyond it.

Employing the new two-variable engine control generates significant benefits in helicopter inter-coupled dynamics. On the one hand, the fluctuations of the controlled variables (see Fig. 11k–n) are more dissipated now than those of the traditional control scheme, on the other hand, the control burden is now far more lightened (see Fig. 11a, o).

5.3 Robustness of the New Engine Control in Autorotation Power Recovery

It is meaningful to note that the control effects in other envelope points (near the trimmed state $V_x^g < 20$) are similar, so those plots are no more given here. The simulation results exemplified above show that the designed two-variable control law presented in this paper is suitable for different working states. Due to the robust LMI method, once the dynamic differences are bounded, the controllers would guarantee the stability and tracking performance, as proved in section IV. For the entire flight envelope, the robust control law described in this paper is not enough, and some further studies will be needed regarding robustness during the entire envelope.

6 Conclusions

In this paper, an autorotation process is simulated and a corresponding engine control law designed. Meanwhile, an appropriate helicopter and engine model is built including dynamics of the helicopter, nonlinear engine dynamics, rotor speed dynamics and especially an induced velocity model capable of capturing vortex ring characteristics.

In order to adapt to large and fast power variation occurring during autorotation power recovery, a two-variable engine control law is proposed on the basis of an integrated helicopter and engine model. Furthermore, compared to a conventional single-variable fuel flow controller, the new one allows a better helicopter dynamic response during the entire autorotation process, ensuring furthermore that the over droop is not exceeding 3 %.

Moreover, with the LMI pole placement method, the simulation results prove that the new designed control law shows a good robustness in stability and tracking performance.

Acknowledgements The work has been co-supported by the National Natural Science Foundation of China (Grant/Award Number: 51576096) and China Aeronautical Science Foundation (Grant/Award Number: 20142152022).

References

1. Wood, T.: One Engine Inoperative (OEI) and Autorotation for Heavy Lift Rotorcraft System. NASA/CR–2012-216038, August (2012)
2. Fox, R.G.: The history of helicopter safety. In: International Helicopter Safety Symposium, Montréal, QC, Canada, 26–29 September 2005
3. Manwaring, J.C.; Conway, G.A.; Garrett, L.C.: Epidemiology and prevention of helicopter external load accidents. J. Saf. Res. **29**(2), 107–121 (1998)
4. Houston, S.S.: Analysis of rotorcraft flight dynamics in autorotation. J. Guid. Control Dyn. **25**(1), 3–39 (2002)
5. Houston, S.S.; Brown, R.E.: Rotor-wake modelling for simulation of helicopter flight mechanics in autorotation. J. Aircr. **40**(5), 938–945 (2003)
6. Kim, H.Y.; Sheen, D.J.; Park, S.O.: Numerical simulation of autorotation in forward flight. J. Aircr. **46**(5), 1642–1648 (2009)
7. Leishman, J.G.: Principles of Helicopter Aerodynamics. Cambridge Aerospace Series, Chap. 5, 2nd edn. Cambridge University Press, Cambridge (2006)
8. Chen, C.: Development of a simplified inflow model for a helicopter rotor in descent flight. Doctoral Dissertation, School of Aerospace Engineering, Georgia Institute of Technology, August (2006)
9. Dalamagkidis, K.; Valavanis, K.P.; Piegl, L.A.: Nonlinear model predictive control with neural network optimization for autonomous autorotation of small unmanned helicopters. IEEE Trans. Control Syst. Technol. **19**(4), 818–831 (2011)
10. Johnson, W.: Helicopter Optimal Descent and Landing after Power Loss. NASA, TM 73244, May (1977)
11. Aponso, B.L.; Lee, D.; Bachelder, E.N.: Evaluation of a rotorcraft autorotation training display on a commercial flight training device. J. Am. Helicopter Soc. **52**(2), 123–133 (2007)
12. Okuno, Y.; Kawachi, K.; Azuma, A.; Saito, S.: Analytical prediction of height-velocity diagram of a helicopter using optimal control theory. J. Guid. Control Dyn. **14**(2), 453–459 (1991)
13. Zhao, Y.; Jhemi, A.A.; Ghent, R.T.N.: Optimal vertical takeoff and landing helicopter operation in one engine failure. J. Aircr. **33**(2), 337–346 (1993)
14. Okuno, Y.; Kawachi, K.: Optimal control of helicopter following power failure. J. Guid. Control Dyn. **17**(1), 181–186 (1994)

15. Carlson, E.B.; Xue, S.; Keane, J.; Burns, K.: H-1 upgrades height-velocity diagram development through flight test and trajectory optimization. In: Proceedings of the American Helicopter Society 62nd Annual Forum, American Helicopter Soc., Alexandria, VA, pp. 729–742 (2006)
16. Bibik, P.; Narkiewicz, J.: Helicopter optimal control after power failure using comprehensive dynamic model. J. Guid. Control Dyn. **35**(4), 1354–1361 (2012)
17. Marconi, L.; Naldi, R.: Robust full degree-of-freedom tracking control of a helicopter. Automatica **43**, 1909–1920 (2007)
18. Garavello, A.; Benini, E.: Preliminary study on a wide-speed-range helicopter rotor/turbo-shaft system. J. Aircr. **49**(4), 1032–1038 (2012)
19. Simplicio, P.; Pavel, M.D.; van Kampen, E.; Chu, Q.P.: An acceleration measurement-based approach for helicopter nonlinear flight control using incremental nonlinear. Control Eng. Pract. **21**, 1065–1077 (2013)
20. Chen, S.-W.; Chen, P.-C.; Yang, C.-D.; Jeng, Y.-F.: Total energy control system for helicopter flight/propulsion integrated controller design. J. Guid. Control Dyn. **30**(4), 1030–1039 (2007). doi:10.2514/1.26670
21. Avanzini, G.; Thomson, D.; Torasso, A.: Model predictive control architecture for rotorcraft inverse simulation. J. Guid. Control Dyn. **36**(1), 207–217 (2013)
22. Shanthakumaran, P.; Harding, J.; Thompson, T.; Kuehn, M.; Monroe, D.: Flight simulation model application for AH-64A Apache engine integration. In: The 49th Annual Forum of the American Helicopter Society, AHS. St. Louis, pp. 261–282 (1993)
23. Smith, B.; Zagranski, R.: Next generation control system for helicopter engines. In: 57th Annual Forum of AHS, Washington, DC, USA, 9–11 May, pp. 1617–1626 (2001)
24. Paramour, M.G.; Jennings, P.D.: Operational requirements for helicopter engine for UK services. In: 82nd Symposium Propulsion and Energetic Panels on Technologies Requirements for Small Gas Turbines at Canada, October 4–8, AGARD-CP-537 (1993)
25. Chilali, M.; Gahinet, P.: H_∞ design with pole placement constraints: an LMI approach. IEEE Trans. Autom. Control **41**(3), 358–367 (1996)
26. Rami, M.A.; El Faiz, S.; Benzaouia, A.; Tadeo, F.: Robust exact pole placement via an LMI-based algorithm. IEEE Trans. Autom. Control **54**(2), 394–398 (2009)
27. Howlett, J.: UH-60A Black Hawk engineering simulation program. Volume 1: mathematical model. NASA166309 (1981)
28. Ballin, M.G.: Validation of a Real-Time Engineering Simulation of the UH-60A Helicopter. NASA Technical Memorandum 88360, February (1987)
29. Wenrong, Y.: Research on integrated modeling, control and optimization of turboshaft engine/rotor. Doctoral Dissertation, College of Energy and Power, Nanjing University of Aeronautics and Astronautics, P. R. China, June (2008)
30. Padfield, G.D.: Helicopter Flight Dynamics—The Theory and Application of Flying Qualities and Simulation Modelling, Chap. 2, Chap. 3. Blackwell Science LTD, Hoboken (1996)
31. Jianguo, S.; Vasilyev, V.; Ilyasov, B.: Advanced Multivariable Control Systems of Aeroengines, Chap. 2, 1st edn. Beijing University of Aeronautics and Astronautics press, Beijing (2005)
32. Ballin, M.G.: A High Fidelity Real-Time Simulation of a Small Turboshaft Engine. NASA TM I0W991, July (1988)
33. Duyar, A.; Gu, Z.; Litt, J.S.: A simplified dynamic model of the T700 turboshaft engine. J. Am. Helicopter Soc. **40**(4), 62–70 (1995)
34. Adibhatla, S.; Brown, H.; Gastineau, Z.: Intelligent Engine Control (IEC), ALASA 92–384. In: 28th Joint Propulsion Conference Exhibit. Nashville, TN (1992)
35. Wang, J.; Ye, Z.; Hu, Z.: Nonlinear control of aircraft engines using a generalized Gronwall-bellman lemma approach. J. Eng. Gas Turbines Power **134**, 094502-1–094502-6 (2012)
36. Slotine, J.J.; Li, W.: Applied Nonlinear Control, Chap. 4. Prentice Hall Englewood Cliffs, Upper Saddle River (1991)
37. Houston, S.S.: Validation of a non-linear individual blade rotorcraft flight dynamics model using a perturbation method. Aeronaut. J. **98**(977), 260–266 (1994)